Joule

CellPress

Article

Long-Range Charge Extraction in Back-Contact Perovskite Architectures via Suppressed Recombination

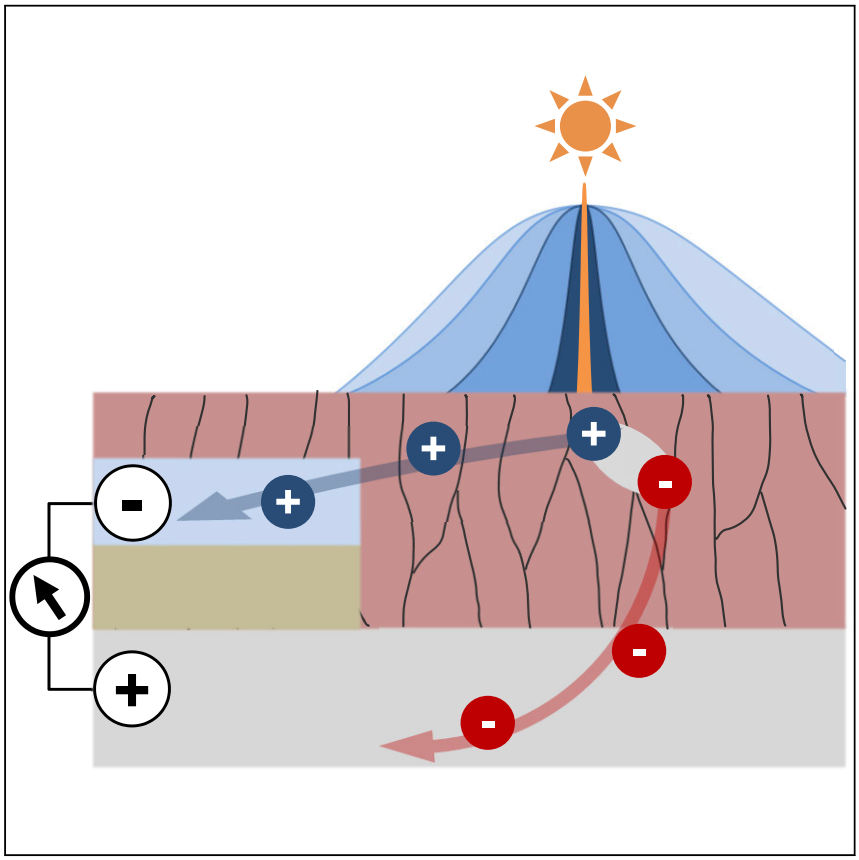

A detailed understanding of charge transport is vital to maximize the efficiencies of optoelectronic devices. Using a back-contact architecture, the authors probe transport of electrons and holes separately in polycrystalline hybrid perovskite thin films. Isolating photoexcited charge carriers in separate regions of the device leads to long diffusion ranges of carriers. The authors demonstrate a back-contact perovskite solar cell that operates on majority-carrier diffusion. These results highlight electrode interfaces as limiting aspects of current back-contact architectures, indicating opportunities for improvement.

Gregory D. Tainter, Maximilian T. Hörantner, Luis M. Pazos-Outón, ..., Henry J. Snaith, Hannah J. Joyce, Felix Deschler

fd297@cam.ac.uk

HIGHLIGHTS

Back-contact device efficiency is driven by majority carrier diffusion

Electrode-induced spatial segregation of charge carriers increases diffusion range

Diffusion lengths exceed 12 μm in thin-film back-contact architecture devices

Electron diffusivity is twice that of holes for polycrystalline $MAPbI_3$ films

Tainter et al., Joule *3*, 1301–1313
May 15, 2019
https://doi.org/10.1016/j.joule.2019.03.010

Joule

CellPress

Article

Long-Range Charge Extraction in Back-Contact Perovskite Architectures via Suppressed Recombination

Gregory D. Tainter,[1,2] Maximilian T. Hörantner,[3,5] Luis M. Pazos-Outón,[4] Robin D. Lamboll,[2] Haralds Āboliņš,[2] Tomas Leijtens,[3,6] Suhas Mahesh,[3] Richard H. Friend,[2] Henry J. Snaith,[3] Hannah J. Joyce,[1] and Felix Deschler[2,7,*]

SUMMARY

Metal-halide perovskites are promising solution-processable semiconductors for efficient solar cells with unexpectedly high diffusion ranges of photogenerated charges. Here, we study charge extraction and recombination in metal-halide perovskite back-contact devices, which provide a powerful experimental platform to resolve electron- or hole-only transport phenomena. We prepare polycrystalline films of perovskite semiconductors over laterally separated electron- and hole-selective materials of SnO_2 and NiO_x. Upon illumination, electrons (holes) generated over SnO_2 (NiO_x) rapidly transfer to the buried collection electrode, leaving holes (electrons) to diffuse laterally as majority carriers in the perovskite layer. Under these conditions, we find recombination is strongly suppressed. Resulting surface recombination velocities are below 2 cm s^{-1}, approaching values of high-quality silicon. We find diffusion lengths exceed 12 μm, an order of magnitude higher than reported in vertically stacked architectures. We fabricate back-contact solar cells with short-circuit currents as high as 18.4 mA cm^{-2}, reaching 70% external quantum efficiency.

INTRODUCTION

Metal-halide perovskites hold great promise as cost-effective, solution-processable thin-film semiconductors for use in solar cells,[1] light-emitting diodes (LEDs),[2] photodetectors,[3] and lasers.[4,5] Design of high-efficiency devices requires an understanding of charge transport lengths and recombination rates. In LEDs, the distance charges travel limits device dimensions, while non-radiative recombination reduces solar cell device efficiency. Furthermore, electrons and holes are subject to different effective masses, recombination processes, and scattering phenomena, so device design must take into account transport and recombination characteristics of each species. In the classic semiconductors, gallium arsenide and silicon, transport dynamics of the two different charge carrier types were examined in doped *n*- and *p*-type materials.[6,7] In halide perovskites, however, excess charge tends to be compensated by intrinsic defects or mobile ions; thus, no substitutional or chemical doping has been achieved to date. Similarly, though some success has been achieved with *n*-type field-effect transistors (FETs), field-effect mobilities are low and likely compromised by ionic screening.[8] Thus, it has proven challenging to measure electron-specific and hole-specific charge transport properties in perovskite materials. In this regard, metal-halide perovskites have been compared to chalcopyrites,[9] which also possess electrically active defects resulting in high compensation ratios.[10]

Context & Scale

Metal-halide perovskites are promising sustainable low-cost materials for optoelectronic devices such as solar cells and LEDs. To optimize performance in these applications, a detailed understanding of charge transport characteristics and the influence of interfaces, such as grain boundaries, is vital. At present, a wide range of transport parameters have been reported, often via indirect measurements, since direct measurement has proven challenging. Here, we demonstrate an approach based on measurements in a back-contact geometry that is capable of probing electron and hole transport mechanisms separately. Such insights are not typically accessible in vertical architectures. We demonstrate a back-contact perovskite device, which we find to operate by majority-carrier diffusion and find that charges diffuse remarkable distances in such scenarios. Diffusion over remarkably long distances over electron-extraction electrodes enables efficient charge collection in short-circuit conditions.

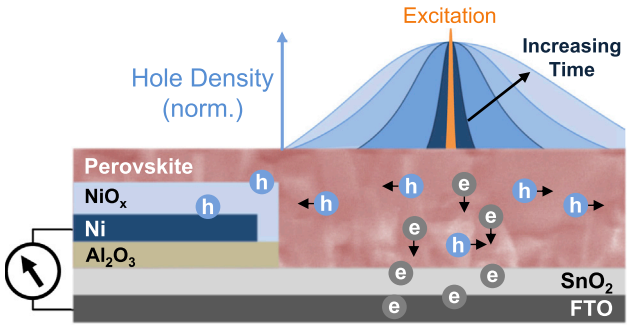

Figure 1. Schematic of Investigated Architecture and Spatially-Resolved Charge Transport Detection

Charge-selective layers NiO_x and SnO_2 extract photogenerated holes/electrons, respectively, leaving the opposite charge in the halide perovskite. Here, charges are photoexcited in the perovskite layer over SnO_2 a certain distance from the NiO_x-SnO_2 electrode junction. Blue curves represent the development of hole population with time after initial excitation, where majority charge carriers diffuse radially until charge generation balances charge recombination and extraction to reach steady-state conditions. Dark blue curves correspond to early times, while light blue curves approach steady-state conditions.

Here, we perform measurements of electron-specific and hole-specific transport in perovskites by exploiting a back-contact solar cell architecture. To date, most perovskite solar cell development has focused on vertical "sandwich" architectures, while the highest-performing silicon technologies are based on back-contact devices.[11] Back-contact architectures rely on efficient lateral transport of photogenerated carriers across the absorber layer to alternating hole- and electron-selective contacts distributed on the rear side of the device. Non-radiative recombination of charge carriers negatively impacts photovoltaic device performance in two ways: it lowers the operating and open-circuit voltages,[12] and it reduces the number of carriers available for extraction. Low recombination and high diffusivities in crystalline silicon allow for electrodes as wide as 1 mm,[13] whereas grain boundaries in polycrystalline materials can present obstacles for efficient charge diffusion and therefore require shorter spacings.[14] Studies on single-crystal lead-halide perovskites have reported charge diffusion lengths exceeding 30 μm, reaching 320 μm for majority carriers in low-injection conditions.[15,16] Diffusion lengths in polycrystalline devices are lower, roughly 1 μm in vertical devices.[17,18] Recent reports modeled diffusion lengths of over 70 μm based on charge lifetimes exceeding 30 μs achieved in uncontacted polycrystalline films with improved passivation techniques.[19] We show here that unexpectedly long diffusion lengths can be achieved in contacted perovskite films in back-contact devices. Back-contact architectures remove the requirement for a transparent top electrode, providing two potential benefits: higher currents due to improved light trapping and more flexibility in processing and passivation treatments.

We prepare contacted thin film structures by depositing polycrystalline methylammonium lead triiodide ($MAPbI_3$) on charge-selective hole- and electron-conducting layers NiO_x and SnO_2, respectively. Figure 1 provides a schematic of the sample architecture and the setup used for our measurements (fabrication details in the Supplemental Information). The metal-halide perovskite layer has a thickness of ~300 nm, with topographical features every ~500 nm (Figures 4B and S1). As shown in Figure 1, optical excitation of $MAPbI_3$ deposited over SnO_2 will result in electron extraction by the electron-selective SnO_2 electrode, leaving holes to diffuse as the majority carrier in the perovskite layer and vice versa over NiO_x. Under operation, we thereby achieve regions with excess *n*- and *p*-type carriers in the perovskite layer

[1]Centre for Advanced Photonics and Electronics (CAPE), Electrical Engineering Division, University of Cambridge, Cambridge CB3 0FA, UK

[2]Cavendish Laboratory, University of Cambridge, Cambridge CB3 0HE, UK

[3]Clarendon Laboratory, Department of Physics, University of Oxford, Oxford OX1 3PU, UK

[4]Department of Electrical Engineering and Computer Sciences, University of California Berkeley, Berkeley, CA 94720-1770, USA

[5]Present address: Research Laboratory of Electronics, Massachusetts Institute of Technology, 77 Massachusetts Avenue, Cambridge, MA 02139, USA

[6]Present address: National Renewable Energy Laboratory, 15013 Denver West Parkway, Golden, CO 80401, USA

[7]Lead Contact

*Correspondence: fd297@cam.ac.uk

https://doi.org/10.1016/j.joule.2019.03.010

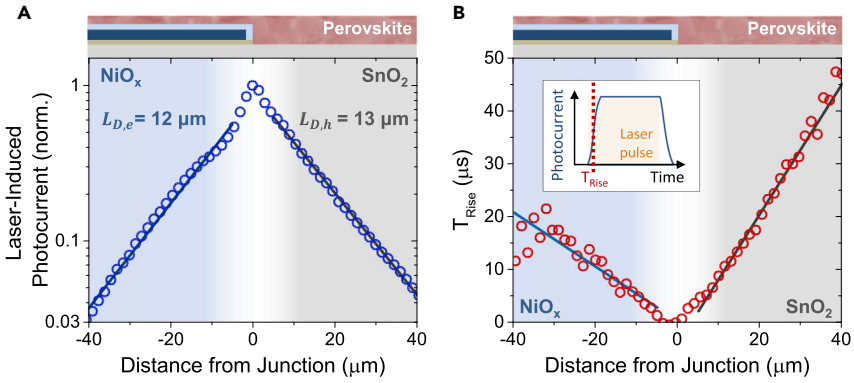

Figure 2. Determination of Charge Transport Characteristics via Photocurrent Spectroscopy

Dependence of photocurrent (A) and rise time (B) with distance from the electrode junction. The photocurrent decays exponentially with distance from the electrode junction, yielding characteristic charge diffusion lengths of $L_{D,electrons}$ = 12 μm, and $L_{D,holes}$ = 13 μm. By fitting to a diffusion model (details in Supplemental Information and Lamboll and Greenham[21]), charge carrier recombination velocity (v) and diffusion constant (D) are extracted: v_{NiO_x} = 1.7 cm s^{-1} and v_{SnO_2} = 1.1 cm s^{-1}/ $D_{electrons}$ = 0.13 cm^2 s^{-1} and D_{holes} = 0.07 cm^2 s^{-1}. The inset to (B) presents the evolution of photocurrent with time under illumination (the orange area represents illumination time) with characteristic rise time T_{Rise}, which is quantified from the photocurrent phase measured by a lock-in amplifier. Measurement performed using an average power of 400 nW, corresponding to a local excitation density of ~80 suns (spot size 1.5 μm).

over the NiO_x and SnO_2 electrode materials, respectively. This device architecture therefore allows us to probe how electrons and holes diffuse and recombine within contacted polycrystalline perovskite devices to gain information that is not accessible in vertical architectures.

RESULTS

Probing Charge Transport via Photocurrent Microscopy

We use scanning photocurrent and photoluminescence (PL) microscopy[15,20] to resolve charge population dynamics and transport in $MAPbI_3$ films at short circuit, which prevents the development of a lateral electric field. A chopped light source is focused on a local area (~1.5 μm) of the film, and the resulting photocurrent amplitude and phase are measured with high sensitivity using a lock-in amplifier. Upon local excitation, generated charges diffuse until steady-state conditions are reached (light blue curve, Figure 1). The temporal response of the photocurrent (inset, Figure 2B) is determined by the diffusion constant and recombination rate of the electrical carriers. The phase delay between the chopped excitation and the photocurrent signal is used to determine a characteristic photocurrent rise time.

To investigate how far charges travel in our device, photocurrent amplitude is measured while varying the distance between the excitation spot and the NiO_x–SnO_2 junction (Figure 2A). The measured photocurrent follows an exponential decay with increasing excitation-junction distance, both when exciting over NiO_x or SnO_2. We extract the electron and hole carrier diffusion lengths for this device from exponential fits to the data (details of the diffusion models given in Supplemental Information), which yield values of $L_{D,electrons}$ = 12 μm, and $L_{D,\ holes}$ = 13 μm. Near the position of the junction, we observe a deviation from expected mono-exponential decay of photocurrent. This could be due to optical edge effects, inconsistencies in film thickness, or field effects at the junction, for which reason we exclude the central region in our fits. The amount of photocurrent collected over the two regions differs, with 40% more photocurrent collected over SnO_2 than over NiO_x at 40 μm excitation-junction distance.

We note that in either direction, over 3% of peak photocurrent is still collected at distances of 40 μm. This suggests that grain boundaries, which occur every ~500 nm in the investigated system, do not prevent charge diffusion.

We investigate the temporal evolution of carrier populations from the photocurrent rise time versus distance (Figure 2B). The rise time increases linearly with distance, as expected, since the phase of the lock-in amplifier measures the signal onset time, not the arrival time of the integrated photocurrent.[21] Excitation over SnO_2 (*p*-type perovskite) results in larger values of rise time than excitation over NiO_x (*n*-type perovskite). This indicates that holes take a longer time to travel to the electrode junction, indicative of a lower diffusion coefficient. Summarizing photocurrent results, both photocurrent amplitude and rise time are higher over SnO_2, indicating that holes diffuse more slowly than electrons and that charges moving over SnO_2 recombine at a lower rate.

To quantify diffusivities and carrier lifetimes from our photocurrent measurements, we use a reported diffusion model that accounts for the radial diffusion of generated charge carriers.[21] This model maps the complex radial diffusion problem presented in our measurements to one dimension and translates the measured photocurrent phase to the photocurrent transport time (details in the Supplemental Information). By using the results of photocurrent amplitude and rise time, the diffusion constant, D, and rate of recombination, k, can be calculated. It is has been proposed that surface recombination dominates for perovskite thin films,[22] but photocurrent measurements are unable to distinguish between recombination mechanisms. Therefore, we report an effective surface recombination velocity of carriers diffusing laterally through the perovskite film, assuming recombination at one interface is dominant. Effective surface recombination velocity (v) is presented assuming a film thickness (h) of 300 nm (v=hk). We find effective surface recombination velocities of $v_{NiO_x} = 1.7\ (\pm\ 0.5)\ cm\ s^{-1}$ and $v_{SnO_2} = 1.1\ (\pm\ 0.3)\ cm\ s^{-1}$, as well as diffusivities of $D_{electrons} = 0.13\ (\pm\ 0.05)\ cm^2\ s^{-1}$ and $D_{holes} = 0.07\ (\pm\ 0.03)\ cm^2\ s^{-1}$. Notably, the surface recombination velocity in the operating quasi-interdigitated back-contact (QIBC) devices is very low compared with isolated "non-contacted" materials,[23–25] approaching well-passivated crystalline silicon, where surface recombination values as low as 0.25 cm s^{-1} have been reported.[26] Comparing presented surface recombination velocities to the film thickness (h) to calculate carrier lifetime (τ_l), $\tau_l = \frac{h}{v}$, we find majority-carrier lifetimes of 27 μs for holes in $MAPbI_3$ over the SnO_2 electrode and 17 μs for electrons over the NiO_x electrode.

Electrode-Induced Charge Segregation

To investigate the origin of the low recombination rate over the electrode materials, we perform photoluminescence quantum efficiency (PLQE) experiments on $MAPbI_3$ films prepared over electrode materials and on glass. When $MAPbI_3$ is deposited over electrode materials, the quantum yield is reduced (Table 1). This PL quenching suggests either (1) increased interfacial non-radiative recombination or (2) charge segregation, which would lower radiative rates because of reduced overlap of electron and hole populations and hence increase the competitiveness of non-radiative recombination channels. While we find a higher rate of recombination over NiO_x in contact measurements (Figure 2), we find less PL quenching in the case of $MAPbI_3$ on NiO_x than on SnO_2.

To investigate further recombination and the origin of PL quenching, we measure time-correlated single-photon counting (TCSPC) PL of $MAPbI_3$ films prepared over

Table 1. Carrier Recombination Parameters over Electrode Materials

Electrode Material	External PL Quantum Yield	PL(t = 50 ns)/PL(t = 0 ns)
SnO_2	0.18%	0.01
NiO_x	0.48%	0.06
Glass	5.2%	0.17

Photoluminescence yields and TCSPC PL signal 50 ns after excitation on $MAPbI_3$ films deposited over SnO_2, NiOx, and glass surfaces. The lower PL yields of $MAPbI_3$ deposited over SnO_2 and NiO_x are correlated with significant initial decay over the first 50 ns after excitation. $MAPbI_3$ deposited over SnO_2 exhibits the largest level of PL quenching. PLQE measurements were performed at ~1 sun (75 mW cm^{-2}, 532 nm). PLQE and TCSPC measurements were performed on large spot sizes on isolated films at open-circuit conditions.

electrode materials and on glass (Figure 3A). In all samples, we find an initial drop in PL intensity in the first ~50 ns after excitation, after which the PL intensity decays at a much slower rate with a lifetime of the order of 1 μs. The magnitude of the initial drop varies significantly between samples, with the initial drop being most pronounced for the films prepared on electrode materials. This observation agrees with our hypothesis of quenching by charge transfer to the buried electrode. The return to a long-lived component of PL lifetime, however, is more surprising. This long-lived process demonstrates that non-radiative interface recombination is not the primary driver of PL quenching in our system since such a recombination process would continue after 50 ns. Our results imply that after ~50 ns, the number of charges being extracted by electrode materials is equal to the number of charges flowing back into the $MAPbI_3$. The PL intensity at 50 ns after excitation (Table 1) over SnO_2 is reduced by a factor of ~6 relative to the case of NiO_x. This implies a larger spatial charge segregation in the case of excitation over SnO_2 (more complete extraction of electrons), which further reduces PL intensity. We suggest that the driving force for segregation is the built-in field at the electrode junction,[27] which our results suggest is larger over SnO_2.

Figure 3B presents predicted steady-state carrier population distributions for varying excitation distances to the electrode junction, which illustrates the changes in electron and hole population overlap. For this visualization, a one-dimensional model that incorporates two-particle diffusion,[21] extraction, and monomolecular and bimolecular recombination is used (details presented in Supplemental Information). Most injected electrons (dashed lines) are extracted by the electrode material. Populations of both charges are present only at the point of excitation, while a relatively high density of holes (>10^{15} cm^{-3}) is present within 40 μm of the excitation spot. In the case of excitation near the electrode junction, holes have only a short distance to travel to the junction, and the resulting buildup of generated carriers at the point of excitation is reduced relative to excitation further from the electrode junction. We observe that the efficient extraction and separation of charge carriers reduces the chance for radiative recombination, and therefore, photon recycling[28] will play a limited role outside the point of excitation.

EFFICIENT CHARGE COLLECTION UNDER OPERATING CONDITIONS

In order to investigate the potential of this device architecture and the potential to harvest carriers with long extraction lengths, we fabricate QIBC devices.[29,30] Instead of continuous sheets of electrode materials, interdigitated NiO_x fingers are deposited over a 3 × 3 mm active area. The distance between fingers varies from 1 to 10 μm (Figures 4A and 4B). The current-voltage characteristics of the QIBC device under AM 1.5 conditions (Figure 4C) shows a short-circuit current density (J_{SC}) of 18.4 mA cm^{-2}, which is the highest J_{SC} reported to date for a perovskite

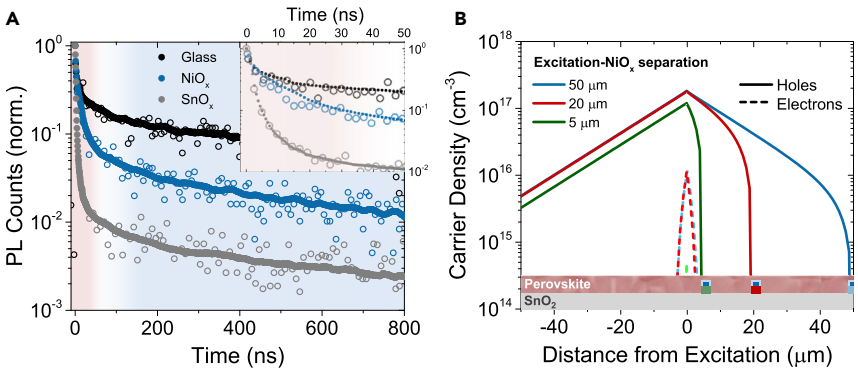

Figure 3. Charge Segregation Effects on Time-Resolved Photoluminescence Measurements and Predicted Device peration

(A) Time-resolved photoluminescence measurements for $MAPbI_3$ films on glass (black), NiO_x on nickel (blue), and SnO_2 on FTO (gray). Data are presented in open circles together with smoothed curves. The decay in photoluminescence shows two regimes: (1) a fast decay in the initial ~50 ns and (2) a long-lived decay approaching similar lifetimes (fits detailed in Table S2). The inset focuses on the early decay of PL intensity. Over SnO_2 and NiO_x materials, the fast decay is more pronounced, with the largest rate of PL decay observed in $MAPbI_3$ deposited over the electron-extracting material SnO_2. The long lifetime component in the case of SnO_2 and NiO_x approaches the long lifetime observed in $MAPbI_3$ deposited on glass (see also Figure S7; Table S2). Measurements were performed at excitation fluences of 5 nJ cm^{-2}.

(B) Modeled steady-state charge distribution for excitation-junction separations of 5 (green), 20 (red), and 50 μm (blue) for excitation over the electron-extracting layer. In the model, excitation is centered at 0 μm distance, and no hole extraction occurs at negative distances. Hole populations are represented by solid lines, and electron populations are represented by dashed lines. Increasing the distance to the extraction point increases the accumulation of charges away from the electrode junction. Details of model parameters are provided in Table S1.

back-contact device.[29,31,32] These high short-circuit current values agree with the low recombination velocities found in Figure 2. The device's power conversion efficiency (PCE) reaches 4.1%, which is limited by a fill factor (FF) of 38% and an open-circuit voltage (V_{OC}) of 0.57 V. These values are mainly affected by substantial dark leakage (or shunting) current, indicative of an imperfect shunt resistance, which may be caused by the imperfection of the Al_2O_3 insulator.

Figure 4D shows the variation of photocurrent and PL over a 30 μm subsection of the active area of a device with 10 μm pitch. Illumination over the NiO_x fingers provides higher PL intensity but reduced photocurrent, while illumination between fingers, over SnO_2, has the opposite effect. Here, we observe a difference in photocurrent behavior to that presented in Figure 2A. In Figure 4D, photocurrent peaks between junctions, in the middle of the SnO_2 region, while in Figure 2A, photocurrent peaks toward the electrode junction. Figure 2 presents measurements over quasi-infinite electrodes of each type, while the limited area of electrodes measured in Figure 4D likely limits charge extraction. This argument is supported by TRPL results in Figure 3A, where charge segregation is more pronounced over SnO_2, and by the marked effect of electrode geometry on charge collection as evidenced in Figure S9. In Figure 4D, photocurrent is dominated by the fast extraction of electrons over SnO_2, compared to slower extraction of holes over NiO_x, where limited NiO_x surface area results in increased charge accumulation. Therefore, the shape of the photocurrent in Figure 4D is limited by charge collection rather than charge transport, resulting in a higher PL intensity and lower photocurrent over NiO_x fingers.

The reported short-circuit current of 18.4 mA cm^{-2} highlights the possibility for efficient charge collection in halide-perovskite solar cells with a QIBC architecture.

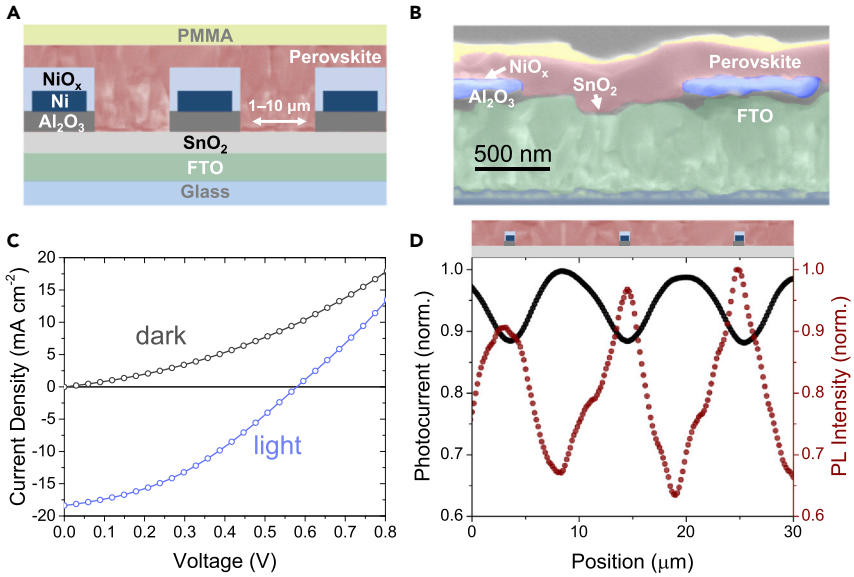

Figure 4. Quasi-Interdigitated Back-Contact Devices with High Short-Circuit Current

(A) Schematic of QIBC solar cell cross section. An electron-selective SnO_2 layer covers FTO-coated glass, and hole-selective fingers, composed of a Ni core with a NiO_x shell, are electrically isolated from SnO_2 with an Al_2O_3 layer. $MAPbI_3$ was spin coated over this structure and topped with PMMA. The NiO_x contacts are 1 μm wide.

(B) Colorized SEM of the device cross section; see also Figure S6.

(C) JV curve of QIBC device with NiO_x finger separation of 1 μm. (PCE = 4.1%, FF = 0.38, V_{OC} = 0.57 V, J_{SC} = 18.4 mA cm^{-2}). See also Figure S8.

(D) Variation in photoluminescence intensity and photocurrent over the active area of a device with 10 μm separation between NiO_x electrodes. PL and photocurrent intensity is anti-correlated, though shape and magnitude in variation remain distinct. The <15% variation in photocurrent over the 10 μm pitch distance demonstrates that charges generated over either electrode have similar collection efficiencies.

See also Figures S3 and S4.

However, the high dark leakage current in our devices under applied bias require improvements in electrode fabrication. Although effort is clearly required for further optimization of cell fabrication, there appears to be no fundamental reason why rear QIBC perovskite cells cannot achieve FFs and open-circuit voltages comparable with the state-of-the-art sandwich-structure devices, with the advantage of the feasibility of delivering a higher short-circuit current, ultimately leading to improved efficiency.

DISCUSSION

We have presented photocurrent and PL measurements revealing remarkably long-range charge transport in contacted polycrystalline metal-halide perovskite films. We use time-resolved photocurrent measurements to extract diffusion lengths of more than 12 μm and effective surface recombination rates as low as 2 cm s^{-1}. These findings are supported by transient PL measurements, which reveal that one charge type (electrons or holes) is removed by the selective contacts, allowing rejected carriers remaining in the perovskite thin film to travel large lateral distances before contributing to photocurrent. Finally, we have demonstrated back-contact perovskite devices that rely on this long-range carrier diffusion for efficient operation. The observed high short-circuit current demonstrates that efficient charge extraction is achieved, which will be improved by increasing the PLQEs through further passivation.

Our results explore the fundamental performance of a back-contact perovskite device. State-of-the-art silicon back-contact devices are developed using doped single crystals, and therefore, device dimensions are limited by the distances over which minority carriers can be harvested. A large range of diffusion ranges have been reported for perovskite materials, stretching from several μm to several hundreds of μm.[15] As Hodes and Kamat noted in the case of single crystal studies,[33] one reason for this is measurement of systems in which one majority carrier is isolated, which allows the isolated charge to travel large distances, even hundreds of micrometers for $MAPbI_3$ single crystals.[16] The long diffusion lengths reported here are the result of reaching quasi-doped situations for electrons and holes separately within the thin film. Furthermore, the dominance of photo-induced excitation over intrinsic carrier concentration combined with selective charge extraction results in a device that is limited by the majority carrier diffusion length of each carrier. Thus, as opposed to minority-limited charge collection in silicon back-contact solar cells, we present a device where majority carrier diffusion limits charge collection.

Our findings have implications toward understanding broader phenomena in metal-halide perovskites and solar cells. One such phenomenon is photo-induced halide migration in halide perovskite materials,[34–36] the origin of which remains under debate. We find that electron diffusivities are roughly twice that of hole diffusivities in polycrystalline $MAPbI_3$. The difference in charge carrier diffusivity likely leads to an excess of holes at the point of excitation, which would result in a radial field under steady-state, point excitation conditions. We therefore expect any ion migration under these fields to be reversible after the excitation is removed.

Furthermore, while the spread of reported transport parameters is partially due to variation in measurement architecture, the quality and crystallinity of perovskite materials have a large impact. Specifically, the effect of perovskite polycrystallinity on device performance remains an active area of investigation, with reports using spatially resolved PL to study whether grain boundaries impede charge transport.[37,38] While precisely quantifying perovskite grain sizes is known to be challenging,[39] we perform measurements of photocurrent at excitation-junction separations much larger than topographical feature size and find that large fractions of excited carriers travel across multiple grain boundaries. This demonstrates that grain boundaries are not major impediments to charge motion in the polycrystalline $MAPbI_3$ films that we have studied here, although investigating a range of different film types would shed more light on the preparation route dependency of this observation.

Fundamentally, the diffusivity of electrons/holes ($D_{e,h}$) is related to the effective carrier mass (m*) and momentum relaxation time (τ) by $D_{e,h} = k_B T \frac{\tau_{e,h}}{m^*_{e,h}}$, where k_B is the Boltzmann constant and T is the carrier temperature. Our measured diffusivity values translate to a ratio $\frac{\tau}{m^*}$ that is ~2 times larger for electrons than holes. Reports using ultrafast spectroscopy provide an upper bound for diffusivity values. Values reported for reduced carrier effective mass ($m^*_e = 0.14 m_0$ where m_0 is the free electron mass)[40] and carrier scattering times ($\tau_{e,h}$= 80 fs)[41] predict diffusivities of 25 $cm^2\ s^{-1}$ on ultrafast timescales before phonon scattering and morphology start to play a role. These values are much higher than the diffusivities obtained from our charge transport experiments or from other longer-range transport measurements.[17,18] This suggests that, on timescales beyond the nanosecond regime, scattering rates (due to phonons, impurities, grain boundaries, etc.)[42] increase.

Our results show that charge segregation effectively improves charge collection and reduces recombination at short-circuit conditions. While the interfaces between perovskite absorber layers and charge extraction materials are expected to contribute significantly to current and open-circuit voltage losses,[43] we show that carriers can move across perovskite-NiO_x and perovskite-SnO_2 interfaces with unexpectedly low losses. For these IBC devices, improved fabrication to reduce the dark saturation current is expected to improve V_{OC} to beyond 1 V, and improved optical design and charge extraction will increase the photocurrent toward 27 mA cm^{-2}. By further combining the low recombination velocities demonstrated here with improved perovskite passivation via chemical treatment[44] and compositional tuning,[45,46] highly efficient IBC perovskite devices will be achievable.

EXPERIMENTAL PROCEDURES

Substrate Preparation

The glass substrates have been purchased from Pilkington Inc. with a coated fluorinated tin oxide (FTO) layer of 7 or 15 Ω/*sq*. FTO was partially removed from the substrate via etching with zinc powder and 2 M HCl to create non-conductive stripes for later needed counter-electrode fabrication. The etched substrates were rinsed in deionized (DI) water and cleaned rigorously by brushing Hellmanex solution with a toothbrush before rinsing again in a stream of DI water. N_2 was used to dry the substrates that were then subsequently rinsed in acetone and 2-propanol and then etched for 10 min in O_2 plasma.

Spin-Coated and Chemical-Bath-Treated SnO_2 *n*-Type Layer

The SnO_2 layer was prepared by following the method described by Anaraki et al.[47] 0.05 M $SnCl_4 \cdot 5H_2O$ was dissolved over 30 min of stirring in 2-propanol and then spin coated in volumes of 200 μL onto the cleaned and etched FTO-coated glass substrates at 3,000 rpm for 30 s with 200 rpm/s acceleration. The substrates were then dried for 10 min at 100°C and 60 min at 180°C. In the meanwhile, a chemical bath was prepared by mixing 40 mL DI water with 500 mg urea, 500 μL HCl (37 wt %), 10 μL of 3-mercaptopropionic acid, and 108 mg $SnCl_2 \cdot 2H_2O$ (for a final concentration of 0.012 M). The cooled down, spin-coated substrates were then immersed into the chemical bath to be well covered by solution, and a lid was placed onto the beaker to prevent evaporation. The bath was kept at 70°C within an oven for 180 min, and afterward, the samples were sonicated for 2 min in DI water. The substrates were dried under a stream of dry air and then put onto a hotplate at 180°C for 60 min.

Photoresist Patterning

The image reversal photoresist AZ 5214 E was spin coated at 5,000 rpm for 45 s and baked for 50 s at 110°C according to the datasheet provided by the manufacturer. UV-light exposure with a wavelength of 265 nm and 25 mJ intensity through a chrome patterned glass photomask and subsequent image reversal, by baking for 120 s at 120°C and applying a 250 mJ dose of UV exposure, led to the solubility of the regions designed for the fingers of the rear contacts. These were dissolved through immersion for roughly 40 s in a developer bath of AZ 726 MIF, resulting in a patterned photoresist layer.

Al_2O_3 + Ni + NiO_X Shell Hole-Conducting Electrode

The patterned photoresist layer was coated with 100 nm insulating Al_2O_3 and 100 nm nickel through e-beam evaporation. The thicknesses of each layer were established using calibrated microbalances during evaporation. The lift-off of the remaining photoresist regions was performed in an 80°C heated bath of dimethyl

sulfoxide (DMSO). The Ni-based devices were subsequently annealed at 300°C for 20 min to create a shell of oxidized Ni as a *p*-type electron blocking layer.

Perovskite Layer Deposition for Back-Contact Solar Cells

For back-contact solar cells, the 3:0.98:0.02 molar ratio of CH_3NH_3I:$PbCl_2$:PbI_2 was well dissolved in DMF with a concentration of 38.5 wt % and spin coated onto the substrates with patterned electrodes at 2,000 rpm for 45 s in a dry air atmosphere. The drying of the deposited solution was performed under a weak air flow for 30 s before letting the substrates rest for 15 min at room temperature and an additional drying step for 15 min at 70°C on a hotplate. The films were then annealed in an oven for 90 min at 100°C and 15 min at 120°C. After the perovskite annealing procedure and the cooling of the substrates to room temperature, a layer of poly(methyl methacrylate) (PMMA) was deposited by spin coating a solution of 15 mg PMMA, dissolved in 1 mL chlorobenzene, at 2,000 rpm for 45 s. Resulting perovskite films have topographical features occurring every ~500 nm. While SEM cannot determine exact grain size,[39] resulting perovskite films have topographical features occurring every ~500 nm (SEMs provided in Figures S1 and S5).

Perovskite Layer Deposition for Films

Perovskite films were prepared on three types of substrates: glass, NiO_x-Ni-glass, and SnO_2-FTO-glass. In the case of films deposited on electrode materials, the electrodes were prepared as described above for devices, save for nickel being evaporated directly onto glass as opposed to on Al_2O_3. The perovskite film was accomplished first by dissolving a 3.05:1 molar ratio of CH_3NH_3I to $Pb(CH_3CO_2)_2 \cdot 3\,H_2O$ into DMF with a concentration of 48 wt %. Solutions were then spin coated onto substrates at 4,000 rpm for 30 s in a nitrogen-filled glovebox. The films were then annealed on a hotplate for 15 min at 100°C. After the perovskite annealing procedure and the cooling of the substrates to room temperature, a layer of PMMA was deposited by spin coating a solution of 15 mg PMMA, dissolved in 1 mL chlorobenzene, at 4,000 rpm for 30 s.

Device Testing

The devices were illuminated from the PMMA side with AM 1.5 simulated sunlight (ABET Technologies Sun 2000, calibrated with NREL certified KG5 filtered Si reference diode). Devices, in air at 20°C, were light soaked for ~1 min at 1 Sun and then measured with a Keithley 2400 in forward and reverse bias voltage scan direction. Scans were performed at 0.38 V/s with a hold time of 5 s at 1.2 V. The devices were not masked, but the active area was well defined via e-beam lithography, which established the photomask and covered an area of 0.09 cm^2 per device.

Photoluminescence Quantum Efficiency Measurements

The PLQE of the samples was measured using an integrating sphere method, described elsewhere.[48] A continuous wave 532 nm diode laser was used to photo-excite the samples with an intensity of 75 mW cm^{-2}. Emission was measured using an Andor iDus DU490A InGaAs detector. PLQE of each sample was measured at three locations.

Time-Resolved Single-Photon Counting PL Measurements

Two setups were used to perform TCSPC measurements on films. Measurements were performed using a PicoQuant LDH405 pulsed laser (407 nm and excitation pulse length and fluence of 100 ps and 5 nJ cm^{-2}) to excite perovskite films. PL was collected at 90° to the incident beam, passed through a monochromator to select the wavelength, and then into a photomultiplier detector (Hamamatsu R3809U-50). In the case of the TCSPC data acquired on perovskite samples

deposited on SnO_2, measurements were performed using a Fianium WhiteLase High Power Supercontinuum laser (WL-SC-IR-8) using a 10 nm band-pass filter centered at 450 nm to select the excitation wavelength. The excitation pulse length and energy were 6 ps and 5 nJ cm^{-2}, respectively. Light was collected at 30° to the incident beam and passed through a 700-nm-long pass filter to remove the contribution of the excitation.

Microscope PL and Photocurrent Measurements

Combined PL and photocurrent measurements were acquired using a WITec alpha 300 s setup. The excitation source was a 405 nm continuous wave laser (Coherent CUBE), chopped using a Stanford Research SR 540 chopping unit at 810 Hz with a 50% duty cycle. The light was coupled though an optical fiber to the microscope and focused using a 40× Olympus lens (NA = 0.6, spot size 1.5 μm). Samples rested on an X-Y piezo stage of the microscope. The PL signal was collected in reflection mode with the same 40× objective and detected using a Princeton Instruments SP-2300i spectrometer fitted with an Andor iDus 401 CCD detector. A long pass filter with a cutoff wavelength of 450 nm was fitted before signal collection to block the excitation. Example spectra for the different active device regions are provided in Figure S2.

Photocurrent detection was accomplished using micro needle probes, which feed a Stanford Research SR 570 preamplifier. The signal from the preamplifier was detected as current intensity and phase shift using a Stanford Research SR 830 lock-in amplifier (referenced to the chopper frequency). By movement of the sample stage, maps of combined PL and photocurrent were recorded. An example of a map taken over the device active region is provided in Figure S3. Measurements as presented in Figure 2 were performed at the junction of continuous regions of electron- and hole-conducting layers. All measurements are done at short-circuit. All movements of the stage and lenses and all spectral and photocurrent data were recorded using WITec Control 4 software. All measurements were performed in air. All photocurrent and PL data displayed are the result of averaging over 10 scans. Errors on extracted diffusivity and surface recombination velocities correspond to the standard deviation over 8 separate extraction length measurements performed.

Conversion of the measured phase offset ($\Delta\theta$) of photocurrent signal to characteristic rise time was based off the chopping frequency. For 810 Hz chopping frequency, conversion was as follows:

$$\frac{\Delta\theta}{360} \times \frac{1}{810\ Hz} = T_{rise}.$$

Measurements were performed with 50–3,200 nW average illumination power. Measurements presented in Figure 2 were performed at 400 nW average power, while measurements in Figure 4D were performed at 1 μW average power.

DATA AND SOFTWARE AVAILABILITY

The data underlying this publication are available at https://doi.org/10.17863/CAM.37464.

SUPPLEMENTAL INFORMATION

Supplemental Information can be found online at https://doi.org/10.1016/j.joule.2019.03.010.

ACKNOWLEDGMENTS

We acknowledge financial support from the Engineering and Physical Sciences Research Council of the UK (EPSRC). G.D.T. thanks the Nano Doctoral Training Centre (NanoDTC) of the EPSRC, the Cambridge Trusts, and Robinson College (University of Cambridge) for financial support. L.M.P.-O. was supported by the Kavli Energy NanoScience Institute Heising-Simons Junior Fellowship of the University of California, Berkeley, and the NanoDTC of the University of Cambridge. H.Ā. thanks the Winton Programme for the Physics of Sustainability (University of Cambridge) for financial support. H.J.J. acknowledges funding from the European Research Council. (grant no. 716471, ACrossWire) and the Royal Commission for the Exhibition of 1851. F.D. acknowledges funding from a Winton Advanced Research Fellowship. We thank H. Sirringhaus and N.C. Greenham for their support and valuable discussions.

AUTHOR CONTRIBUTIONS

G.D.T., L.M.P.-O., R.D.L., and F.D. conceived the experiments. M.T.H., T.L., and H.J.S. conceived and developed the QIBC device architecture. M.T.H. and S.M. characterized device efficiency and contributed to device optimization. H.Ā. provided films. G.D.T. and H.Ā. performed all other experiments. G.D.T. analyzed the data and performed the presented modeling. All authors discussed the data and contributed to the manuscript, which was written by G.D.T., M.T.H., L.M.P.-O., R.D.L., R.H.F., H.J.S., H.J.J., and F.D.

DECLARATION OF INTERESTS

The authors declare no competing interests.

Received: August 22, 2018
Revised: February 26, 2019
Accepted: March 11, 2019
Published: April 16, 2019

REFERENCES

1. Yang, W.S., Noh, J.H., Jeon, N.J., Kim, Y.C., Ryu, S., Seo, J., and Seok, S.I. (2015). SOLAR CELLS. High-performance photovoltaic perovskite layers fabricated through intramolecular exchange. Science *348*, 1234–1237.

2. Wang, J., Wang, N., Jin, Y., Si, J., Tan, Z.K., Du, H., Cheng, L., Dai, X., Bai, S., He, H., et al. (2015). Interfacial control toward efficient and low-voltage perovskite light-emitting diodes. Adv. Mater. *27*, 2311–2316.

3. Dou, L., Yang, Y.M., You, J., Hong, Z., Chang, W.H., Li, G., and Yang, Y. (2014). Solution-processed hybrid perovskite photodetectors with high detectivity. Nat. Commun *5*, 5404.

4. Xing, G., Mathews, N., Lim, S.S., Yantara, N., Liu, X., Sabba, D., Grätzel, M., Mhaisalkar, S., and Sum, T.C. (2014). Low-temperature solution-processed wavelength-tunable perovskites for lasing. Nat. Mater. *13*, 476–480.

5. Deschler, F., Price, M., Pathak, S., Klintberg, L.E., Jarausch, D.D., Higler, R., Hüttner, S., Leijtens, T., Stranks, S.D., Snaith, H.J., et al. (2014). High photoluminescence efficiency and optically pumped lasing in solution-processed mixed halide perovskite semiconductors. J. Phys. Chem. Lett. *5*, 1421–1426.

6. Runyan, W.R. (1975). Semiconductor Measurements and Instrumentation (McGraw-Hill).

7. Casey, H.C., Miller, B.I., and Pinkas, E. (1972). Variation of minority-carrier diffusion length with carrier concentration in GaAs liquid-phase epitaxial layers. J. Appl. Phys. *44*, 1281–1287.

8. Senanayak, S.P., Yang, B., Thomas, T.H., Giesbrecht, N., Huang, W., Gann, E., Nair, B., Goedel, K., Guha, S., Moya, X., et al. (2017). Understanding charge transport in lead iodide perovskite thin-film field-effect transistors. Sci. Adv. *3*, e1601935.

9. Brenner, T.M., Egger, D.A., Kronik, L., Hodes, G., and Cahen, D. (2016). Hybrid organic-inorganic perovskites: low-cost semiconductors with intriguing charge-transport properties. Nat. Rev. Mater. *1*, 15007.

10. Cahen, D., Abecassis, D., and Soltz, D. (1989). Doping of copper indium selenide ($CuInSe_2$) crystals: evidence for influence of thermal defects. Chem. Mater *1*, 202–207.

11. Yoshikawa, K., Kawasaki, H., Yoshida, W., Irie, T., Konishi, K., Nakano, K., Uto, T., Adachi, D., Kanematsu, M., Uzu, H., et al. (2017). Silicon heterojunction solar cell with interdigitated back contacts for a photoconversion efficiency over 26%. Nat. Energy *2*, 17032.

12. Pazos-Outón, L.M., Xiao, T.P., and Yablonovitch, E. (2018). Fundamental efficiency limit of lead iodide perovskite solar cells. J. Phys. Chem. Lett. *9*, 1703–1711.

13. Lu, M., Bowden, S., Das, U., and Birkmire, R. (2007). Interdigitated back contact silicon heterojunction solar cell and the effect of front surface passivation. Appl. Phys. Lett. *91*, 063507.

14. Mat Desa, M.K.M., Sapeai, S., Azhari, A.W., Sopian, K., Sulaiman, M.Y., Amin, N., and Zaidi, S.H. (2016). Silicon back contact solar cell configuration: a pathway towards higher efficiency. Renew. Sustain. Energy Rev. *60*, 1516–1532.

15. Semonin, O.E., Elbaz, G.A., Straus, D.B., Hull, T.D., Paley, D.W., van der Zande, A.M., Hone, J.C., Kymissis, I., Kagan, C.R., Roy, X., et al. (2016). Limits of carrier diffusion in n-type and p-type $CH_3NH_3PbI_3$ perovskite single crystals. J. Phys. Chem. Lett. *7*, 3510–3518.

16. Dong, Q., Fang, Y., Shao, Y., Mulligan, P., Qiu, J., Cao, L., and Huang, J. (2015). Solar cells. Electron-hole diffusion lengths > 175 μm in

solution-grown $CH_3NH_3PbI_3$ single crystals. Science *347*, 967–970.

17. Stranks, S.D., Eperon, G.E., Grancini, G., Menelaou, C., Alcocer, M.J., Leijtens, T., Herz, L.M., Petrozza, A., and Snaith, H.J. (2013). Electron-hole diffusion lengths exceeding 1 micrometer in an organometal trihalide perovskite absorber. Science *342*, 341–344.

18. Edri, E., Kirmayer, S., Mukhopadhyay, S., Gartsman, K., Hodes, G., and Cahen, D. (2014). Elucidating the charge carrier separation and working mechanism of $CH_3NH_3PbI(3-x)Cl(x)$ perovskite solar cells. Nat. Commun. *5*, 3461.

19. Brenes, R., Guo, D., Osherov, A., Noel, N.K., Eames, C., Hutter, E.M., Pathak, S.K., Niroui, F., Friend, R.H., Islam, M.S., et al. (2017). Metal halide perovskite polycrystalline films exhibiting properties of single crystals. Joule *1*, 155–167.

20. Wilson, T., and McCabe, E.M. (1987). Theory of optical beam induced current images of defects in semiconductors. J. Appl. Phys. *61*, 191–195.

21. Lamboll, R.D., and Greenham, N.C. (2017). Reduced dimensionality in drift-diffusion models of back-contact solar cells and scanning photocurrent microscopy. J. Appl. Phys. *122*, 133106.

22. Yang, Y., Yang, M., Moore, D., Yan, Y., Miller, E., Zhu, K., and Beard, M. (2017). Top and bottom surfaces limit carrier lifetime in lead iodide perovskite films. Nat. Energy *2*, 16207.

23. Nelson, R.J., and Sobers, R.G. (1978). Minority-carrier lifetimes and internal quantum efficiency of surface-free GaAs. J. Appl. Phys. *49*, 6103–6108.

24. Yang, Y., Yan, Y., Yang, M., Choi, S., Zhu, K., Luther, J.M., and Beard, M.C. (2015). Low surface recombination velocity in solution-grown $CH_3NH_3PbBr_3$ perovskite single crystal. Nat. Commun. *6*, 7961.

25. Staub, F., Hempel, H., Hebig, J., Mock, J., Paetzold, U.W., Rau, U., Unold, T., and Kirchartz, T. (2016). Beyond bulk lifetimes: insights into lead halide perovskite films from time-resolved photoluminescence. Phys. Rev. Applied *6*, 1–13.

26. Yablonovitch, E., Allara, D.L., Chang, C.C., Gmitter, T., and Bright, T.B. (1986). Unusually low surface-recombination velocity on silicon and germanium surfaces. Phys. Rev. Lett. *57*, 249–252.

27. Dymshits, A., Henning, A., Segev, G., Rosenwaks, Y., and Etgar, L. (2015). The electronic structure of metal oxide/organo metal halide perovskite junctions in perovskite based solar cells. Sci. Rep. *5*, 8704.

28. Pazos-Outón, L.M., Szumilo, M., Lamboll, R., Richter, J.M., Crespo-Quesada, M., Abdi-Jalebi, M., Beeson, H.J., Vrućinić, M., Alsari, M., Snaith, H.J., et al. (2016). Photon recycling in lead iodide perovskite solar cells. Science *351*, 1430–1433.

29. Jumabekov, A.N., Della Gaspera, E., Xu, Z.-Q., Chesman, A.S.R., van Embden, J., Bonke, S.A., Bao, Q., Vak, D., and Bach, U. (2016). Back-contacted hybrid organic–inorganic perovskite solar cells. J. Mater. Chem. C *4*, 3125–3130.

30. Snaith, H.J., Leijtens, T., Alexander-Webber, J., and Hoerantner, M.T. (2017). Device Architecture. WO Patent 2017/060700 A1.

31. Lin, X., Jumabekov, A.N., Lal, N.N., Pascoe, A.R., Gómez, D.E., Duffy, N.W., Chesman, A.S.R., Sears, K., Fournier, M., Zhang, Y., et al. (2017). Dipole-field-assisted charge extraction in metal-perovskite-metal back-contact solar cells. Nat. Commun. *8*, 613.

32. Jumabekov, A.N., Lloyd, J.A., Bacal, D.M., Bach, U., and Chesman, A.S.R. (2018). Fabrication of back-contact electrodes using modified natural lithography. ACS Appl. Energy Mater *1*, 1077–1082.

33. Hodes, G., and Kamat, P.V. (2015). Understanding the implication of carrier diffusion length in photovoltaic cells. J. Phys. Chem. Lett. *6*, 4090–4092.

34. Barker, A.J., Sadhanala, A., Deschler, F., Gandini, M., Senanayak, S.P., Pearce, P.M., Mosconi, E., Pearson, A.J., Wu, Y., Srimath Kandada, A.R., et al. (2017). Defect-assisted photoinduced halide segregation in mixed-halide perovskite thin films. ACS Energy Lett. *2*, 1416–1424.

35. Bischak, C.G., Hetherington, C.L., Wu, H., Aloni, S., Ogletree, D.F., Limmer, D.T., and Ginsberg, N.S. (2017). Origin of reversible photoinduced phase separation in hybrid perovskites. Nano Lett. *17*, 1028–1033.

36. DeQuilettes, D.W., Zhang, W., Burlakov, V.M., Graham, D.J., Leijtens, T., Osherov, A., Bulović, V., Snaith, H.J., Ginger, D.S., and Stranks, S.D. (2016). Photo-induced halide redistribution in organic-inorganic perovskite films. Nat. Commun. *7*, 11683.

37. Ciesielski, R., Schäfer, F., Hartmann, N.F., Giesbrecht, N., Bein, T., Docampo, P., and Hartschuh, A. (2018). Grain boundaries act as solid walls for charge carrier diffusion in large crystal Mapi thin films. ACS Appl. Mater. Interfaces *10*, 7974–7981.

38. DeQuilettes, D.W., Jariwala, S., Burke, S., Ziffer, M.E., Wang, J.T., Snaith, H.J., and Ginger, D.S. (2017). Tracking photoexcited carriers in hybrid perovskite semiconductors: trap-dominated spatial heterogeneity and diffusion. ACS Nano *11*, 11488–11496.

39. Adhyaksa, G.W.P., Brittman, S., Āboliņš, H., Lof, A., Li, X., Keelor, J.D., Luo, Y., Duevski, T., Heeren, R.M.A., Ellis, S.R., et al. (2018). Understanding detrimental and beneficial grain boundary effects in halide perovskites. Adv. Mater. *30*, e1804792.

40. Price, M.B., Butkus, J., Jellicoe, T.C., Sadhanala, A., Briane, A., Halpert, J.E., Broch, K., Hodgkiss, J.M., Friend, R.H., and Deschler, F. (2015). Hot-carrier cooling and photoinduced refractive index changes in organic-inorganic lead halide perovskites. Nat. Commun. *6*, 8420.

41. Richter, J.M., Branchi, F., Valduga de Almeida Camargo, F., Zhao, B., Friend, R.H., Cerullo, G., and Deschler, F. (2017). Ultrafast carrier thermalization in lead iodide perovskite probed with two-dimensional electronic spectroscopy. Nat. Commun. *8*, 376.

42. Wolfe, C.M., Stillman, G.E., and Lindley, W.T. (1970). Electron mobility in high-purity GaAs. J. Appl. Phys. *41*, 3088–3091.

43. Sandberg, O.J., Sundqvist, A., Nyman, M., and Österbacka, R. (2016). Relating charge transport, contact properties, and recombination to open-circuit voltage in sandwich-type thin-film solar cells. Phys. Rev. Applied *5*, 044005.

44. DeQuilettes, D.W., Koch, S., Burke, S., Paranji, R.K., Shropshire, A.J., Ziffer, M.E., and Ginger, D.S. (2016). Photoluminescence lifetimes exceeding 8 μs and quantum yields exceeding 30% in hybrid perovskite thin films by ligand passivation. ACS Energy Lett. *1*, 438–444.

45. Saliba, M., Matsui, T., Domanski, K., Seo, J.Y., Ummadisingu, A., Zakeeruddin, S.M., Correa-Baena, J.P., Tress, W.R., Abate, A., Hagfeldt, A., et al. (2016). Incorporation of rubidium cations into perovskite solar cells improves photovoltaic performance. Science *354*, 206–209.

46. Abdi-Jalebi, M., Andaji-Garmaroudi, Z., Cacovich, S., Stavrakas, C., Philippe, B., Richter, J.M., Alsari, M., Booker, E.P., Hutter, E.M., Pearson, A.J., et al. (2018). Maximizing and stabilizing luminescence from halide perovskites with potassium passivation. Nature *555*, 497–501.

47. Anaraki, E.H., Kermanpur, A., Steier, L., Domanski, K., Matsui, T., Tress, W., Saliba, M., Abate, A., Grätzel, M., Hagfeldt, A., et al. (2016). Highly efficient and stable planar perovskite solar cells by solution-processed tin oxide. Energy Environ. Sci. *9*, 3128–3134.

48. De Mello, J.C., Wittmann, H.F., and Friend, R.H. (1997). An improved experimental determination of external photoluminescence quantum efficiency. Adv. Mater *9*, 230–232.